City and Environment Interactions 19 (2023) 100110

Contents lists available at ScienceDirect

City and Environment Interactions

journal homepage: www.sciencedirect.com/journal/city-and-environment-interactions

Fully automated land surface temperature downscaling based on RGB very high spatial resolution images

Yaser Abunnasr, Mario Mhawej *

Department of Landscape Design and Ecosystem Management, Faculty of Agricultural and Food Sciences, American University of Beirut, Bliss St., Beirut 2020-1100, Lebanon

ARTICLE INFO

Keywords:
Urban heat
Commercial satellite
Modeling
Urban heat island
Thermal comfort
Remote sensing

ABSTRACT

Downscaling is a particularly needed process in many environmental, social and governance applications at the fine scale. The need for an automated and reliable very high spatial resolution downscaling approach is then required. In this paper, a fully-automated open-access downscaling approach was proposed, named HSR-LST. It is based on the High Spatial Resolution (HSR) Red, Green and Blue (RGB) bands collected from commercial and free-to-access satellite images, generating LST values lower than 2-m spatial resolutions. This is based on the Landsat-8 thermal datasets and while implementing a fully-automated Ordinary Least Squares (OLS) approach. HSR-LST was implemented over Beirut, Boston and Dubai between 2016 and 2018. In comparison to an airborne LST image captured over ElKhorn River in Nebraska, USA, HSR-LST showed an AME of 0.88 °C and a R-squared value of 86.33%. Main results showed the variability of LST based on the sensed land features' type. Different LST distribution footprints (i.e., irregular in Beirut, intermitted in Boston, systematic in Dubai) were highlighted depicting a characteristic urban configuration in each city. This latter along buildings' material, density and height appear also to show a different effect on the local and surrounding LST values. By implementing the automated HSR-LST model in cities around the Globe, urban planners, policy makers and inhabitants can acquire improved information to assess urban heat islands, to propose more adequate planning policies, but more importantly to tackle urban heat and thermal comfort at the finest scales. HST-LST will effectively address the low spatial resolution of thermal bands. As HSR-LST is both automated and dynamic, it can be portable to other urban areas with diverse climatic regions.

Introduction

Downscaling, disaggregation and spatial sharpening designate similar approaches aimed to increase the spatial resolution of an input image based on higher resolution auxiliary data [76,24,20,31,68]. The importance of downscaling lies in improving the understanding of our surroundings at the finest scale possible, particularly for products that are not suitable for regional applications [54]. This is particularly true where coarse scale satellite sensors can only measure a composite response from multiple available sub-classes. Thus, for instance, at the periphery zone between urban and vegetation areas, urban and non-urban sub-pixels can be seen as a single category pixel [1]. This is where the downscaling procedure is required to determine the fractions and the locations of each of the subcategories present in any coarse pixel. While downscaling approaches are being continuously developed and enhanced, Land Surface Temperature (LST) appears to be one of the most studied variables in the spatial sharpening studies, particularly due to inherited low spatial resolution and diverse applicability in many areas, including urban heat fluxes and configurations (e.g., [9,70]), urban heat islands (e.g., [64,33,2]), wildfires and forest health (e.g., [50,12,39], crop water consumptions and evapotranspiration rates (e.g., [47,45,5], droughts and desertification (e.g., [23,22,67], among many others.

The successive launch of new satellite thermal sensors and improved image resolution have provided better assessment of LST values across diverse landscapes [20]. This did not halt initiatives to improve the current LST images, as spatial resolutions are still lagging behind the much-needed very high-resolution information. The process of improving the LST spatial resolution have begun with the usage of information available within the one-layer panchromatic band (e.g., [56,35]). Since then, related literature is dominated by two main LST downscaling approaches, namely the physical and the statistical

* Corresponding author.
E-mail addresses: ya20@aub.edu.lb (Y. Abunnasr), mm278@aub.edu.lb (M. Mhawej).

https://doi.org/10.1016/j.cacint.2023.100110
Received 7 March 2023; Received in revised form 2 May 2023; Accepted 19 May 2023
Available online 20 May 2023

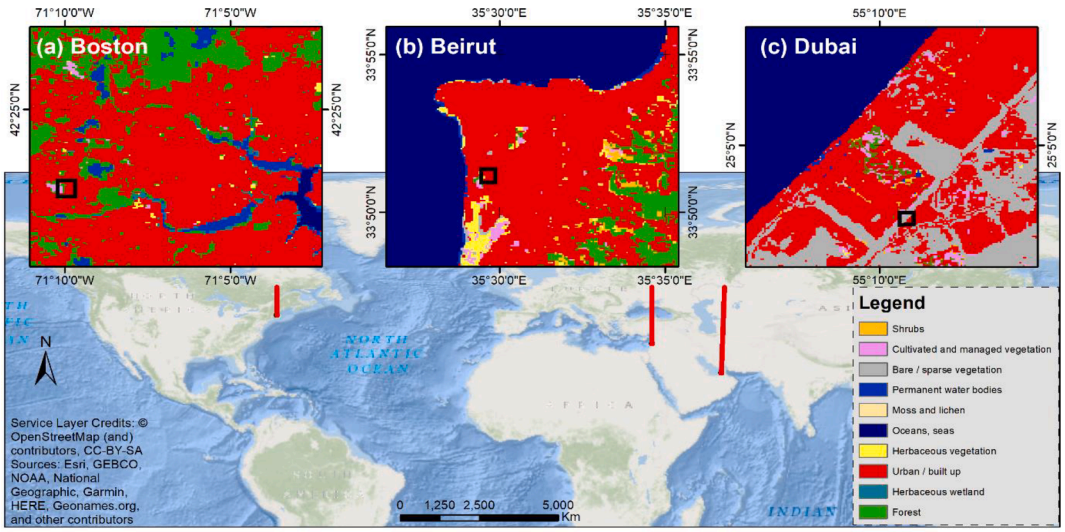

Fig. 1. Location of the studied cities, including from left to right, (a) Boston, (b) Beirut and (c) Dubai; also included the Land Cover map over these regions based on the 100-Copernicus Global Land Cover Layers: CGLS-LC100 Collection 3 in 2019 (black squares refer to the selected study sites).

methods. The first includes the dual band method based on the subpixel thermal anomaly monitoring (e.g., [18,25], as well as the emissivity-based approach founded on the isothermal hypothesis (e.g., [38,77]). On the other hand, statistical downscaling aims at deriving a relationship between LST and auxiliary data, mainly a satellite-based vegetation health. In the latter, the better spatial resolution red and near-infrared bands are used as predictors for the LST variations. More specifically, biophysical vegetation indices are used as predictors, including, but not limited to, the Normalized Difference Vegetation Index (NDVI), the Enhanced Vegetation Index (EVI), the Soil Adjusted Vegetation Index (SAVI), having usually a negative correlation with LST [76]. Here, it is important to note that the negative correlation between daytime LST and vegetation indices may be true for pixels corresponding to terrestrial areas. Under the presence of water or bare lands, the scatterplot appears to have a triangular shape as described by Carlson [11] and Tang et al. [65]. Anyhow, the most adequate vegetation index remains the Fraction of Vegetation Cover (FVC), generated from NDVI, yielding the smallest prediction errors for LST [4]. More recently, Unmanned Aerial Vehicles (UAVs), with its multiple bands and airborne thermal camera observations were used for more accurate thermal mapping and assessments over cities. More likely, a broadband thermal camera is mounted to an airplane (e.g., [63,55] or tethered to a balloon [10]. In comparison to MODerate resolution Imaging Spectroradiometer (MODIS) satellite LST data over a Canadian mining facility, the airborne thermal camera resulted in a median absolute error of 0.64 °C [10]. Furthermore, some previous studies have used the multiple spectral bands of the UAV to conduct a green infrastructure typology (GIT) or a local climate zone (LCZ), providing highly detailed and accurate two- and three-dimensional information much-needed for urban climate analyses at the local scale (e.g., [8,6]. Anyhow, the usage of airborne thermal data remains limited due to its high cost, long acquisition period and extensive data processing requirements [16].

Although widely used, there are limitations to the two dominant downscaling approaches found in the literature. In the physical method, limitations include the requirement of too many independent measurements [18]), whereas, in the statistical approach, using only a biophysical index fails to explain variations in daytime LST at the sub-pixel level, particularly over a heterogeneous landscape [24]. In this context, further studies were conducted to improve these approaches by including the temperature difference between photosynthetically and non-photosynthetically active vegetation (e.g., [44,43]), land cover data (e.g., [66,69,52], fraction of Impervious Surface Area (ISA) (e.g., [75,60], soil water content index (e.g., [73,78], albedo (e.g., [17,72], and elevation data (e.g., [7,30]. Even with the said improvements at the fine scale, implementing these sophisticated approaches [30] as well as ease of transferability to varying regions and contexts [52] still pose challenges related to computation time and memory requirements. Therefore, several algorithms were proposed, based on the previous approaches found in the literature, to automate the downscaling process, including disaggregation procedure for radiometric surface temperature (DisTrad) [36], thermal sharpening (TsHARP) [4], pixel block intensity modulation (PBIM) algorithm [64], high-resolution urban thermal sharpener (HUTS) [17], and data mining sharpener (DMS) [24].

While each previous study attempted to present an innovation in one of the different aspects related to LST downscaling, the similarity in these studies lies in finding relationships between coarser-resolution thermal and other finer-resolution bands produced from the same satellite. More broadly, two directions were identified that define this relationship. The first is related to the use of red and near-infrared bands (e.g., [36,4,32,78] with coarser LST images, whereas the second direction compiles LST images with better spatial but lower temporal resolution imagery for more frequent spatial observations (e.g., [30,27]. The unavailability of fine-scaled LST images, easy processes and models to downscale have resulted in a limited number of LST-based space borne studies (i.e., urban heat island and thermal comfort research) conducted at finer planning scales such as districts and neighborhoods [15].

This study proposes a new direction in the LST downscaling, based on HSR images in urban settings, surnamed HSR LST downscaling approach or HSR-LST. This latter is an adaptive, open-access, fully-automated LST downscaling approach, based on auxiliary data from a different sensor and from non-thermal bands. To our knowledge, no previous study has conducted similar much-needed research for a fine scale analysis. It is important to note, however, that HSR-LST is a fully-automated downscaling model not an LST retrieval model. Thus, it does not process raw L8 images to derive LST, and thus should be produced prior to the implementation of the model.

The selected study area includes portions of three cities (i.e., Beirut, Boston and Dubai) with diverse climates. The newly generated HSR-LST data are based on Landsat-8 (L8) thermal bands, having the best spatially and freely available thermal bands. HSR-LST was developed using one of the most common programming languages (i.e., *python*), and could be implemented, and improved, when necessary, by any interested users to automatically derive reliable urban HSR LST values. It would largely assist urban planners and decision makers across a wide range of related disciplines to better assess urban heat and thermal comfort within the vicinity of cities. The next sections of this paper will

Table 1
HSR images data sources and sensing dates in Beirut, Boston and Dubai.

Location	HSR Image Source	Spatial resolution	Sensing Date
Beirut	Digitalglobe WorldView-2	2-m	July-December 2017
Boston	National Agriculture Imagery Program (NAIP)	1-m	2018
Dubai	Pleiades-1A and 1B	0.5-m	April, May, September 2016 and March 2017

explain and implement the HSR-LST approach in Beirut, Boston and Dubai. It will be followed by a validation of the HSR-LST product against an airborne LST image captured in Nebraska, USA.

Materials and methods

Study area

The study area (Fig. 1) corresponds to three major cities with varied climates, urban morphology, and incident sun radiation. These cities were selected due to our possession of very high spatial resolution satellite images covering it, which also coincides with having different climates and urban configurations. More particularly, Beirut has a hot-summer Mediterranean climate (Csa), Boston has a hot-summer humid continental climate (Dfa) and Dubai has a hot desert climate (BWh), according to Koppen climate classification [53].

The latitude of Beirut is 33°50′N with a population of 1.5 million and an average density of 6,200 inhabitants/km^2 [21]. Altitudes range between 0 and 200 m above sea level. The hot season lasts for approximately four months with average air temperature of 29 °C and relative humidity over 70%.

Municipal Boston, at a latitude of 42°50′N, had an estimated 700,000 inhabitants in 2018, according to the Consolidated Metropolitan Statistical Area (CMSA) of Boston, Massachusetts (MA). The average altitude is 43 m above sea level. The warm season lasts between three and four months with average air temperature of 25 °C and relative humidity of 20%.

The city of Dubai with a latitude of 25°50′N is one of the most known cities in the United Arab Emirates with a staggering 3.3 million population living within the city's boundary. Dubai is roughly at sea level, with a maximum altitude of 16 m above sea level. The hot season lasts between four and five months with average air temperature of 39 °C and relative humidity over 70%. The regions studied in this research correspond to one random site but having multiple Land Cover types over each city with a buffer area of 1 km.

Data background

HSR images were retrieved from different sensors (Table 1). For Beirut, Digitalglobe WorldView-2 was collected between July and December 2017, having eight bands (i.e., coastal blue, blue, green, yellow, red, red-edge, near-infrared-1, and near-infrared-2) at an approximate spatial resolution of 2-m. For Boston, the 2018 1-m National Agriculture Imagery Program (NAIP), with four bands (i.e., blue, green, red and near-infrared) was used. For Dubai, Pleiades-1A and 1B were collected between 2016 and 2017 with a spatial resolution up to 0.5-m with four bands similar to the NAIP.

Since its launch on February 11, 2013, Landsat-8 (L8) satellite has provided 30-m resolution images of the earth surface across different wavelengths every 16 days. The L8 is equipped with two 100-m resolution thermal sensors to assess the earth skin temperatures or the LST. In this study, the readily-available 30-m L8 USGS Surface Reflectance along atmospherically-corrected LST Tier 1 Level 2 products are used. The atmospheric correction corresponds to the Land Surface Reflectance Code (LaSRC) algorithm. The LST datasets found in this product are created with a single-channel algorithm jointly created by the Rochester Institute of Technology (RIT) and National Aeronautics and Space Administration (NASA) Jet Propulsion Laboratory (JPL). Further details on the LST computation from L8 can be available in Faour et al. [23]. L8 Datasets were freely downloaded from the USGS official website (i.e., https://earthexplorer.usgs.gov/).

Table 2
WRS path/row, scene ID and overpass dates of the L8 in Beirut, Boston and Dubai.

Location	WRS Path/Row and Scene ID	L8 Sensing Dates
Beirut	174/36 LC8174036YYYYDDDLGN00	13-Jun-17, 29-Jun-17, 15-Jul-17, 31-Jul-17, 16-Aug-17, 1-Sep-17
Boston	12/30 LC8112030YYYYDDDLGN00	16-Jun-18, 2-Jul-18, 18-Jul-18, 3-Aug-18, 19-Aug-18, 4-Sep-18, 20-Sep-18
Dubai	160/42 LC8160042YYYYDDDLGN00	7-May-16, 23-May-16, 8-Jun-16, 24-Jun-16, 10-Jul-16, 26-Jul-16, 11-Aug-16, 27-Aug-16, 12-Sep-16, 28-Sep-16, 7-Mar-17, 23-Mar-17, 8-Apr-17, 24-Apr-17, 10-May-17, 26-May-17, 11-Jun-17, 27-Jun-17, 13-Jul-17, 29-Jul-17, 14-Aug-17, 30-Aug-17, 15-Sep-17

The timeframe for the study is the hot season in each city and within the same years of the collected HSR images as follows: for Beirut, the months from June to September of 2017; for Boston, between June and September of 2018; and for Dubai between May and September of 2016 and 2017. The median value of the available images for each band of the RGB and in each region was produced. The median value in the hot season is considered as surrogate to the urban heat impact, and has no effect on the HSR-LST calculations and algorithms. The overpass dates of the used L8 LST images in each region is found in Table 2, with a local time of the day ranging between 9:30 a.m. and 10:30 a.m.

To validate the generated product, high-resolution aerial LST images over the lower ElKhorn River and adjacent urban area in Nebraska, USA are used [29]. This dataset includes a georeferenced mosaic of images, presented as a gridded raster image in GeoTiff format. The final image is a 0.5 by 0.5-m grid of corrected surface temperatures (Fig. 2). The dataset encompasses a 16-Km reach of the river, from 0.64-Km upstream from USGS streamflow-gaging station 06800500, Elkhorn River at Waterloo, Nebraska, to 2.9-Km downstream from USGS site 06800800, Elkhorn River at Q St Bridge near Venice, Nebraska. The original usage of these datasets was to interpret groundwater discharge patterns. It was captured on December 15, 2017.

Method

The principle behind the downscaling method used in this study is to build the multiple regression relationship between a dependent variable (i.e., high spatial resolution LST datasets) and independent variables (i.e., Red, Green and Blue (RGB) bands from the very high spatial resolution WorldView-2, NAIP, and Pleiades-1A and 1B images as well as LST images from Landsat 8). It is based on defining probabilities at the sub-pixel level, similar to what was produced in Mhawej et al. [49]. This later research successfully downscaled coarse resolution AMSR-E snow water equivalent from 25-km spatial scale to 500-m using a sub-pixel probability factor based on the frequency of snow days per year, retrieved from the snow cover datasets acquired from 500-m combined MODIS Terra and Aqua satellites. To our knowledge, none of the previous algorithms or studies were developed to include only RGB bands. As such, the HSR-LST is proposed. This is particularly needed because commercial satellites provide these three band types as essential bands while additional bands are provided at additional fees. But also, a prompt and fully-automated downscaling approach dedicated to users from related disciplines is much required for a fine scale assessment and the advancement of related studies. The HSR-LST simplified flowchart is found in Fig. 3.

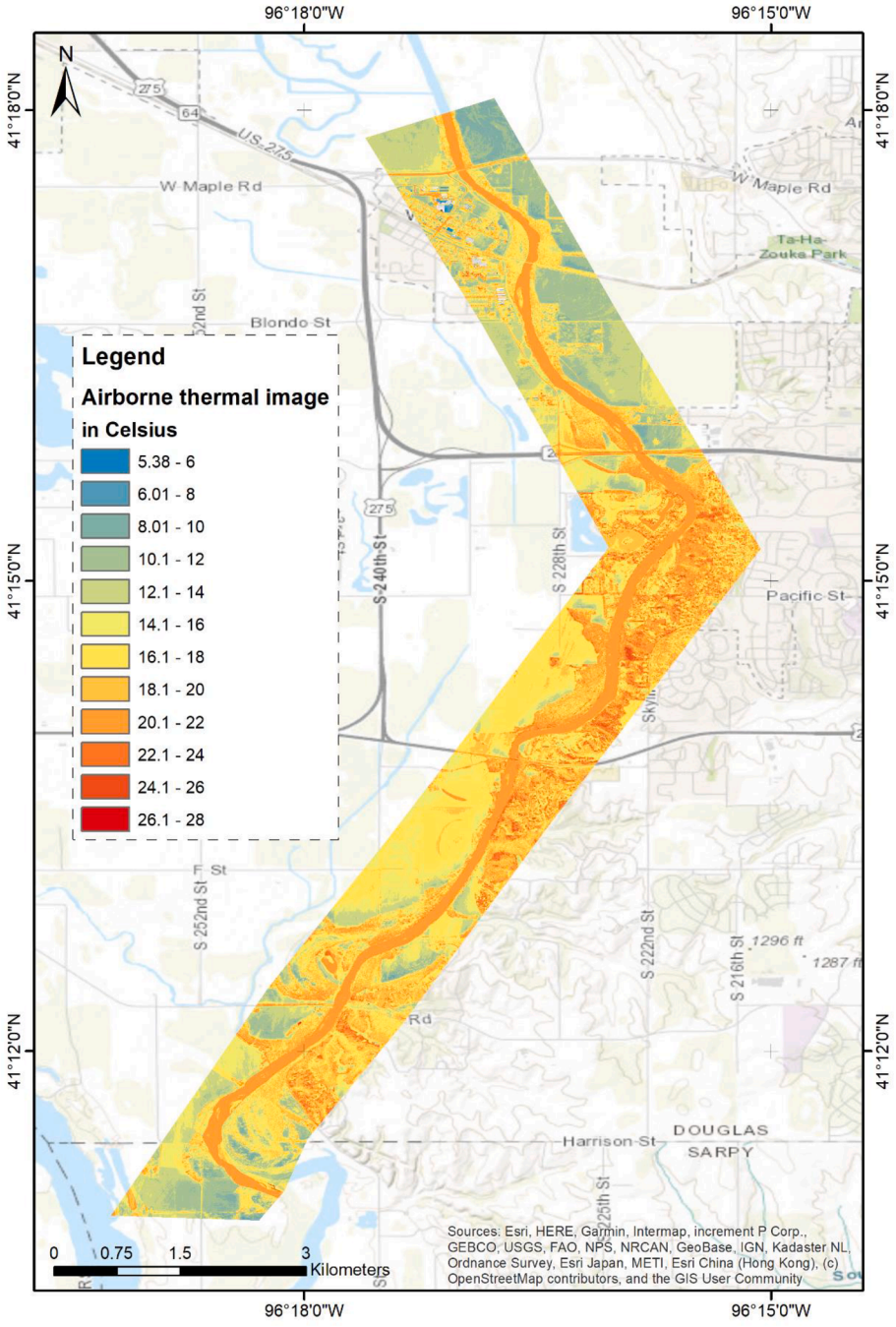

Fig. 2. The lower ElKhorn river airborne LST image used for HSR-LST validation.

Preprocessing approach

Very high spatial resolution images were collected over the study regions, namely 2-m RGB images in Beirut, a 1-m RGB image in Boston and 0.5-m RGB images in Dubai. L8 Level 2 images were also downloaded for the same time periods for each city. Median RGB bands (i.e., bands 2, 3 and 4) from L8 were retrieved in each region and within the hot season. A further processing, not included within HSR-LST, was needed to retrieve the median values within the hot season in each of the three regions.

The HSR-LST approach

The following steps are automatically produced within the HSR-LST model. More particularly, a bandpass adjustment is applied to calibrate HSR RGB and L8 RGB bands as suggested in Claverie et al. [13]. It was based on a linear fit relationship between the red band from an HSR image, for instance, the 1-m NAIP, and the red band from the LSR/L8 image. The same applies for the green and blue bands for each considered city. The linear equations between same band types generated the required slope and intercept to transform the HSR red to LSR/L8 red values, green HSR to green LSR/L8 and blue HSR to blue LSR/L8. Reports were produced to highlight the adjusted R-squared values generated in each of the three linear fit relationships among other accuracy-related tests. Therefore, a new HSR image with updated RGB values is created. It is important to note that an internal processing was made to transform HSR RGB pixel sizes (i.e., being 2-m in Beirut, 1-m in Boston and 0.5-m in Dubai) to the 30-m L8 RGB pixel size using a simple median aggregation technique. Pixel depth type in each HSR image was also changed to correspond to the L8 8-bit unsigned depth type. These fully-

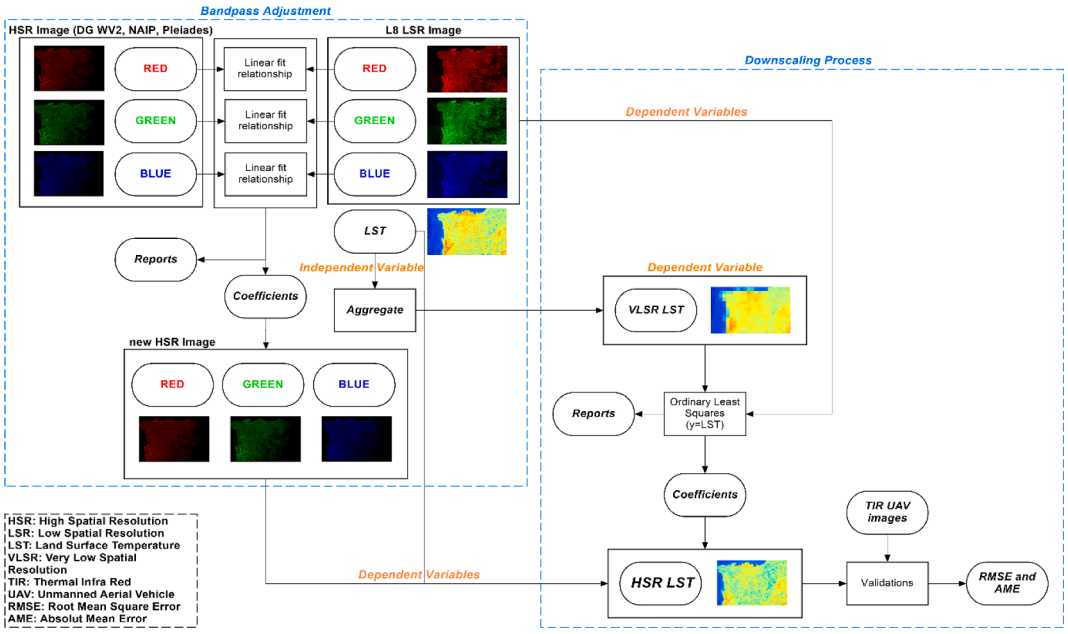

Fig. 3. A simplified flowchart of the HSR-LST method.

automated processes were important to derive relationships at the same spatial scales and over the same pixels' boundaries.

A median aggregation with a cell factor of 30 for the L8 LST images, in each region, is made generating Very Low Spatial Resolution (VLSR) LST images with a spatial resolution of 900-m. This cell factor was used as a surrogate to the ratio between HSR and L8 spatial resolutions. Users have the ability to alter this factor over their regions and check whether this will improve the total accuracy or not.

The Ordinary Least Square (OLS) method is used to estimate the unknown parameters in the linear regression model. L8 RGB bands along the VLSR LST are the independent variables, whereas the L8 LST is the dependent variable. The general equation is as follows:

$$Y = \beta x + \beta' x' + \beta'' x'' + \text{etc.} + \varepsilon.$$

Where Y is the dependent variable;
β, β', β'' are the independent variables;
x, x', x'' are the generated weights;
ε is the interception value.

More particularly, transforming L8 LST into HSR has passed by two intermediary steps; the first is to identify the relationship between L8 LST and a coarse-resolution LST data, namely the VLSR. The second step includes the inverse application of the previously found relationship on HSR and now the coarse-resolution LST datasets, namely the L8 LST. This was done by randomly choosing 3000 points within each city to verify the relationship between the dependent and independent variables, and to determine the level of accuracy. These random points were selected with a minimum distance of 100-m between any two points representing the pixel size of L8 thermal bands. RGB, LST and VLSR LST values were extracted at these points. An OLS test was made between the dependent (i.e., LST) and independent (i.e., red, green, blue, VLSR LST) variables. The coefficients or weights for each independent variable are produced along an interception value. Also, a report highlighting the accuracy of such model is generated based on the adjusted R-squared, Akaike's Information Criterion, Jarque-Bera p-value, Koenker (BP) Statistic p-value, Max Variance Inflation Factor, Global Moran's I p-value tests. Users may adjust values when the produced report shows low accuracy levels by, for instance, changing the cell factor aggregation value in the VLSR LST assessment, increasing the number of randomly selected points in large areas or by eliminating cloudy pixels and then reconduct the OLS assessment.

In the second intermediary step and based on the weighting values retrieved from the previous step, an HSR LST is produced depicting the LST values during the same overpass time of the corresponding L8 images. This latter is considered as the L8/LSR LST in the previously retrieved equation and thus, the dependent variable. The independent variables were the L8/LSR LST and HSR RGB bands. While the scale used in the previous step is 900-m, in this step, the used scale is related to the pixel size of the HSR images, being 2-m in Beirut, 1-m in Boston and 0.5-m in Dubai. For instance, in Beirut, 2500 (i.e., the ratio between 100-m and 2-m in each of the two directions) HSR pixels have the same L8/LSR LST value. What does alter the values of these 2500 sub-pixels is the red, green and blue values collected from the HSR images. In all these tests, the difference in spatial resolution was managed through a resampling towards the higher spatial resolution in each step, even when multiple pixels would have the same value for the coarse resolution images. A registration was followed by aligning pixels from different datasets. All related statistical analysis used are based on the OLS-related tools over ArcMap 10.8 (i.e., Exploratory Regression and Ordinary Least Squares (OLS)).

It is important to note that these steps are fully-automated and are produced under the commonly known *python* programming language, where user only needs to specify the RGB bands from HSR and LSR images as well as the LST layer from the LSR image. The only required library is the arcpy. The open-access full script is available in Annex I.

HSR-LST validation

To validate the generated product, an HSR-LST image was produced for December 2017 over ElKhorn River based on L8 bands, including the surface temperature band, along the NAIP product. It was compared to an airborne LST image captured over ElKhorn River. As the acquisition date is not the same between the L8 LST and the airborne LST, a normalization approach was produced as found in Pu and Bonafoni [57]. More particularly and following a spatial co-registration between the two products, the average 30-m airborne-based LST is computed from the 0.5-m airborne pixels contained in the 30-m L8 LST. It was followed by the generation of the pixel-based LST difference, named dT, subtracting the 30-m airborne LST from the 30-m L8 LST. At a later stage, the dT image was added to the HSR-LST and the average 1-m airborne-based LST was computed from the 0.5-m airborne pixels contained in the

Table 3
RMSE, AME and R-squared HSR LST values compared to L8 LST in Beirut, Boston and Dubai.

	Beirut	Boston	Dubai	Average
RMSE (Kelvin)	0.38	0.8	0.33	0.5
AME (Kelvin)	0.28	0.61	0.25	0.38
R-squared (%)	92.39	88.8	97.21	92.8

1-m HSR-LST.

Over 25,000 points were randomly selected above ElKhorn River. The selected points have a minimum distance of 20-m between any two points. An extraction of the 1-m HSR-LST, with the dT included, and the 1-m airborne LST values were made at these randomly created points. R-squared values, Root Mean Square Error (RMSE) and Absolute Mean Error (AME) were retrieved from the below equations as follows:

$$RMSE = \sqrt{\frac{1}{n}\sum_{i=1}^{n}(Xi - Yi)^2}$$

$$AME = \frac{1}{n}\sum_{i=1}^{n}|Xi - Yi|$$

Where n is the total number of observations, Xi is the ith observed data and Yi is the ith estimated data.

Results

Cross-Evaluation

A comparison between HSR LST and L8 LST values showed very promising RMSE, AME and R-squared values (Table 3). The lowest RMSE, AME and R-squared values were seen in Dubai, with 0.33 Kelvin, 0.38 Kelvin and 97.21%, respectively. Boston, on the other hand, showed the largest error with a RMSE of 0.8 Kelvin, an AME of 0.61 Kelvin and an R-squared value of 88.8%. The average AME and R-Squared values in these selected cities are low (i.e. an AME of 0.38 Kelvin and a R-squared value of 92.8%). Fig. 4 highlights a scatter plot based on the HSR-LST approach in these different cities, along a 1:1 line signaling a 100% correlation. The majority of the values appear to exist in proximity to that line. It is important to note that this scatter plot was established on a large area in each city to capture any variability in values and land cover types.

As shown in Fig. 5, areas of LST values in L8 and HSR images over Beirut, Boston and Dubai were highly overlapped. More particularly, the considered LST values in both data type coincided in 94.88% (i.e. 2839 of 2992 pixels) in Beirut, 94.27% (i.e. 276,503 of 293,294 pixels) in Boston, and 91.33% (i.e. 121,676 of 133,216 pixels) in Dubai.

HSR-LST validation

A comparison between 1-m HSR-LST and 1-m airborne LST values showed very good RMSE (i.e., 1.3 °C), AME (i.e., 0.88 °C) and R-squared values (i.e., 86.33%) (Fig. 6).

HSR-LST implemented in Beirut, Boston and Dubai

Very dense urban areas in Beirut along some tree-covered lands showed one of the least LST, with values around 43 °C in the hot season (Fig. 7, top). Clear high-resolution images showing the patterns of the urban settings can be found in Fig. 8. The highest temperatures were visible in bare and grass lands, where LST values exceeded 45 °C. A vehicular round-about showed an increase of over 1 °C in comparison to its surrounding. Furthermore, the distribution of LST values appears to be irregular. For example, over a swimming pool located at the western part of the city, LST values were the lowest (i.e., less than 38 °C).

In Boston, some of the conclusions are similar to Beirut. More particularly, bare lands showed the highest LST values with over 41 °C in the hot season. A small lake showed the lowest values around 33 °C. The existence of trees, intermitted with houses, enabled a patch-like distribution of LST. The lowest-temperature regions existed far from the main road (Fig. 7, middle).

Dubai showed well-preserved shapes with dominance of LST values over 45 °C in the hot season (Fig. 7, bottom). Bare lands represented very high temperatures of over 53 °C, whereas, houses and their surroundings showed values around 50 °C. Asphalt roads presented less LST values than from bare lands, with values around 52 °C. It was also noticeable the LST values change in terms of different rooftop materials, particularly highlighted in the southern part of the study area.

Furthermore, HSR-LST can be seen refining L8 LST values, related to the HSR images' spatial resolution used. For instance, with the 0.5-m HSR image in Dubai, an unrepresented whole urban area in Landsat is now visible and clearly highlighted. Other spatial improvements were even directly recognized when assessing HSR-LST over Boston, where

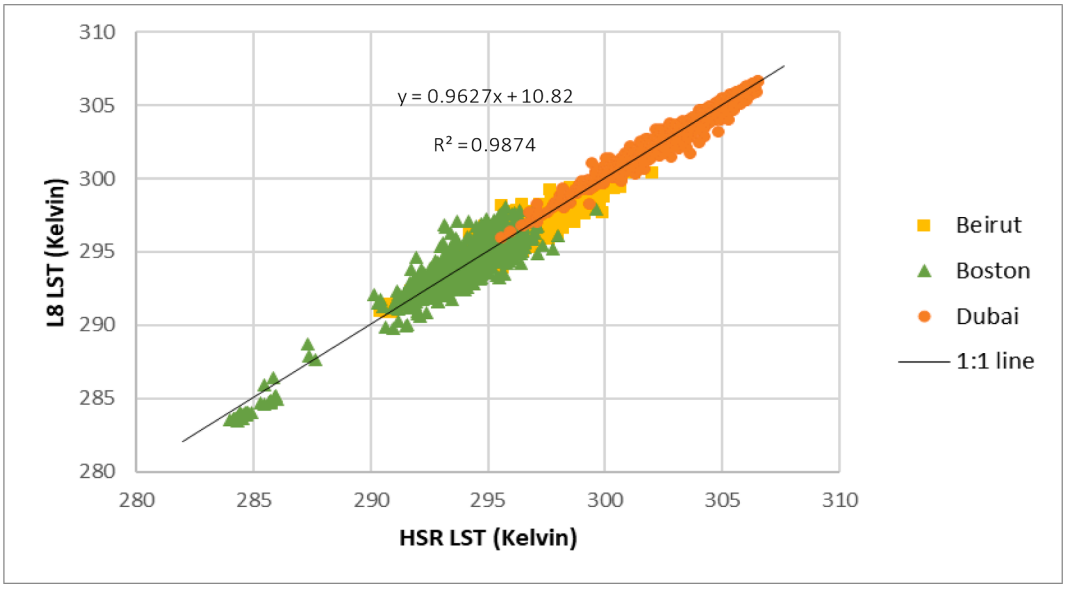

Fig. 4. A scatter plot showing the relationship between the HSR LST and L8 LST values in the three major cities.

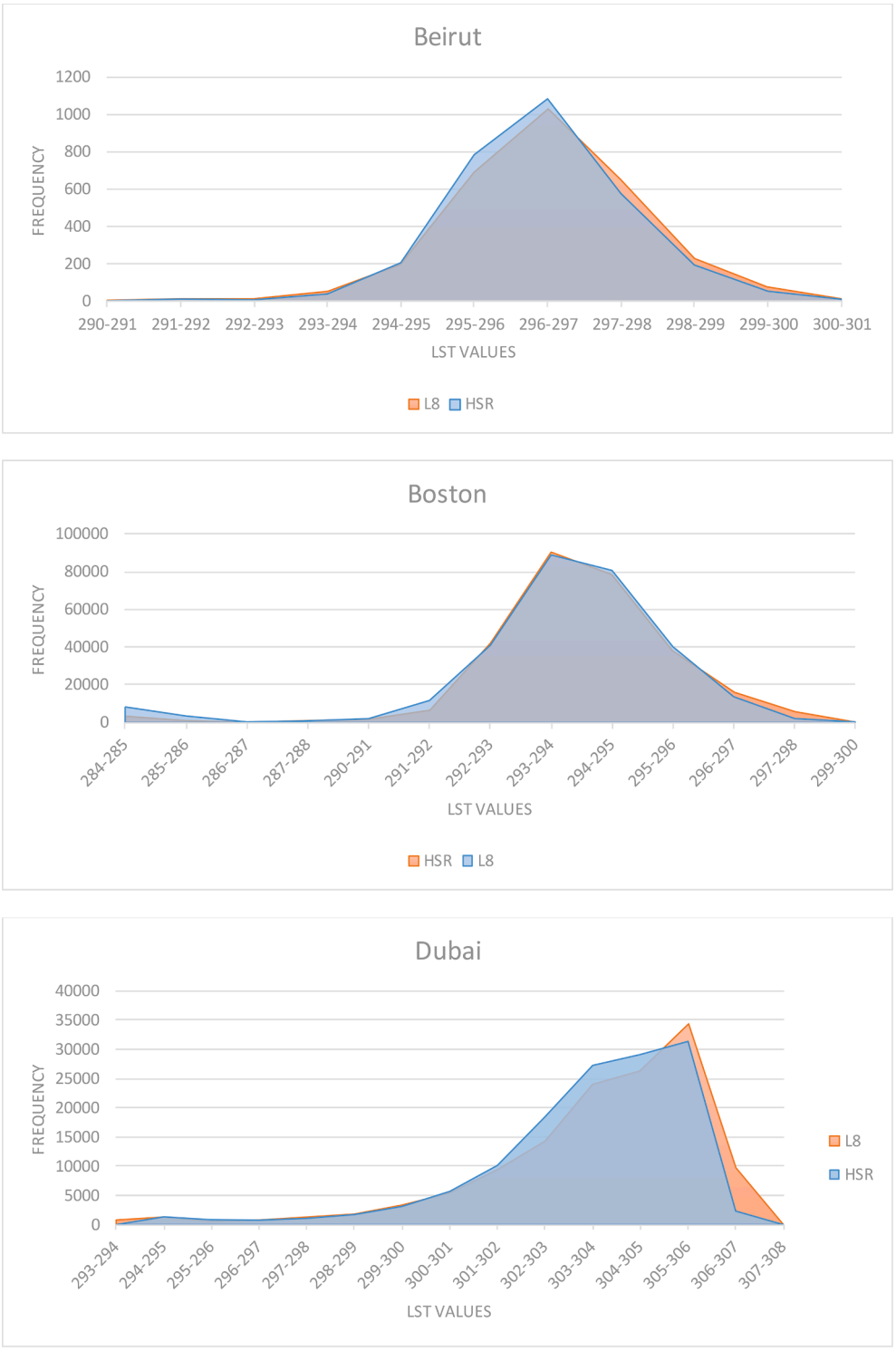

Fig. 5. Areas of LST values' frequency based on L8 and HSR images over Beirut, Boston and Dubai.

the urban agglomeration configuration and water bodies are accurately represented.

Discussion

When validating against an airborne LST image, HSR-LST showed a very promising accuracy which is around the reported 1 °C bias in previous studies (e.g., [59,74,19,37,14,42]. This accuracy was hardly obtained by some previous studies (e.g., [7,24,76,30,72,27]. More recently, Mhawej and Abunnasr [46] and Abunnasr and Mhawej [3] proposed the 10-m Ten-ST-GEE systems, both daily and monthly, and having a better temporal coverage of the suggested HSR-LST system. The reported bias is around 2.3 °C though. A combination between these two systems would enable an improved spatial and temporal resolutions and this would be possible as both Ten-ST-GEE and HSR-LST systems are fully-automated and dynamic.

Anyhow, the results showed some similar characteristics in the selected cities, having diverse climatic regions. More particularly, dense

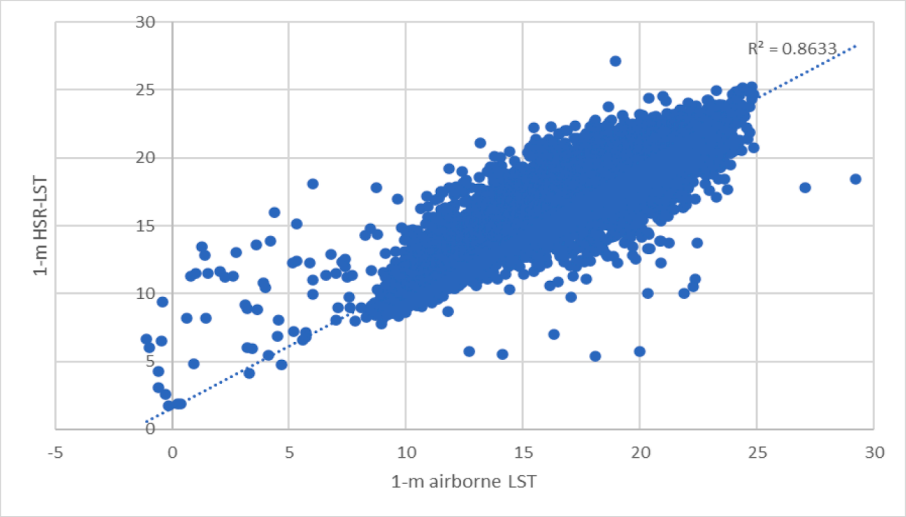

Fig. 6. A scatter plot showing the relationship between the 1-m HSR-LST and 1-m airborne LST values Elkhorn river, Nebraska, USA.

urban fabric showed improved LST values in comparison to their surroundings, which could be related to the blocking of solar radiation due to building density and height as previously suggested by Guo et al. [26]. Tree-covered lands presented a similar outcome, with trees intercepting incoming solar radiation while creating a cooling effect in their lower canopy and understory layers [58,41]. In addition, and as expected, private pools and other water bodies, such as lakes, depicted the lowest LST values in the three cities, where the available water is reducing temperatures through the decrease of sensible heat flux which generates an increase in the evaporation rates ([48,45,5] and therefore reducing LST values.

The highest LST values were seen in bare and grass lands, including vehicular round-about of unplanted lands, where low water content in the upper soil layers and reduced evapotranspiration rates due to the limited vegetation cover are usually observed (e.g., [79,68]. These areas showed an increase of 7 °C in Beirut and 8 °C in Boston in comparison to water body LST values. These temperatures appear to be dissipating to their surroundings. Further assessments should be made to retrieve its impact at each distance from their centers, and if its total area could present any significant change to the nearby LST values. The same goes for the rooftop materials, where LST values differed largely and affected their surroundings which is particularly visible in Dubai.

The different LST distribution footprints (i.e., irregular in Beirut, intermittent in Boston, systematic in Dubai), depicted the existing urban configuration, enabling an accurate representation of urban heating at the neighborhood and city scales. More particularly, few "cold" areas were observed in some part of the selected locations, mainly visible in Boston, enabling later a more in-depth analysis of the LST variations at finer scales. This could not be produced using the 30-m Landsat-8 LST datasets as shown in Fig. 7, where the whole region could be under- or over-estimated.

It is important to note, however, that the proposed approach relies on Landsat-8 images, which can in some cases be partially or fully missing, due to local climate conditions, including clouds. In that case, a data imputation technique could be used such as the Mean Attribute, Most Common Attribute value and k-nearest neighbor imputation [51]. Furthermore, including other LST sensors, such as MODIS, Landsat-9 and Sentinel-3, would largely reduce the reliability on Landsat 8. Still, this would require further analysis to improve the proposed approach and check its validity. Another improvement would include LST data from multiple seasons which should not affect the applicability of the proposed fully automated system but may provide improved accuracy which should be further verified.

While some limitations might appear when implementing a similar approach, this study proposed to retrieve the median value in the hot season in different cities with diverse climates and therefore overcoming the impact of different overpassing periods of the used satellite sensors. Furthermore, the usage of HSR images from diverse sources, having different bands and sensors' characteristics, was important to enable users to implement the proposed approach using any available HSR images, particularly where internal OLS regression reports as well as the final accuracy reports are already embedded in the system.

Anyhow, the proposed HSR-LST provides a new direction in LST downscaling based on HSR RGB images with several contributions to the field allowing for easy use and applicability. The procedure is simple, easy-to-use and freely-available through an automated and open-access python scripting language algorithm. In addition, another importance of this study was to use minimal bands' number to produce reliable high spatial resolution LST. This would be greatly needed for many large-scale studies, as the commercial HSR images come with a limited number of bands, on one hand, and on the other hand, where in some cases the addition of bands would result in staggering data costs. Urban designers, city planners and policy makers would benefit from the generated data to prioritize and develop responsive strategies reducing urban heating at the urban block and neighborhood scales and thus, allowing the possibility to address human comfort at a finer scale rather than the city scale. Furthermore, understanding the current distribution and variations of LST in urban settings will allow the prioritization of urban environmental policies and investments, especially when impacting vulnerable communities. This would also allow the recommendation of specific solutions in specific locations to curb the LST impacts. These may include measures such as changing rooftop material, increasing vegetated cover in urban landscapes, and the redesign of urban configurations in new urban developments or retrofit existing urban neighborhoods. The HSR-LST provides a useful, easy-to-use tool that could steer current and future urban planning and design projects while better integrating urban climates and their dynamics.

Conclusion

Establishing an open-source fully-automated downscaling LST algorithm is a much-needed tool, as LST enters in many environmental and social aspects of everyday human life. The HSR-LST approach has the capability to downscale LST values to an unprecedented very fine spatial resolution, using the RGB bands from HSR images. HSR-LST validation yielded a very reliable accuracy with an AME of 0.88 °C.

HSR-LST showed very high spatial resolution LST values, which is largely based on the retrieval and access to costly HSR images. Further

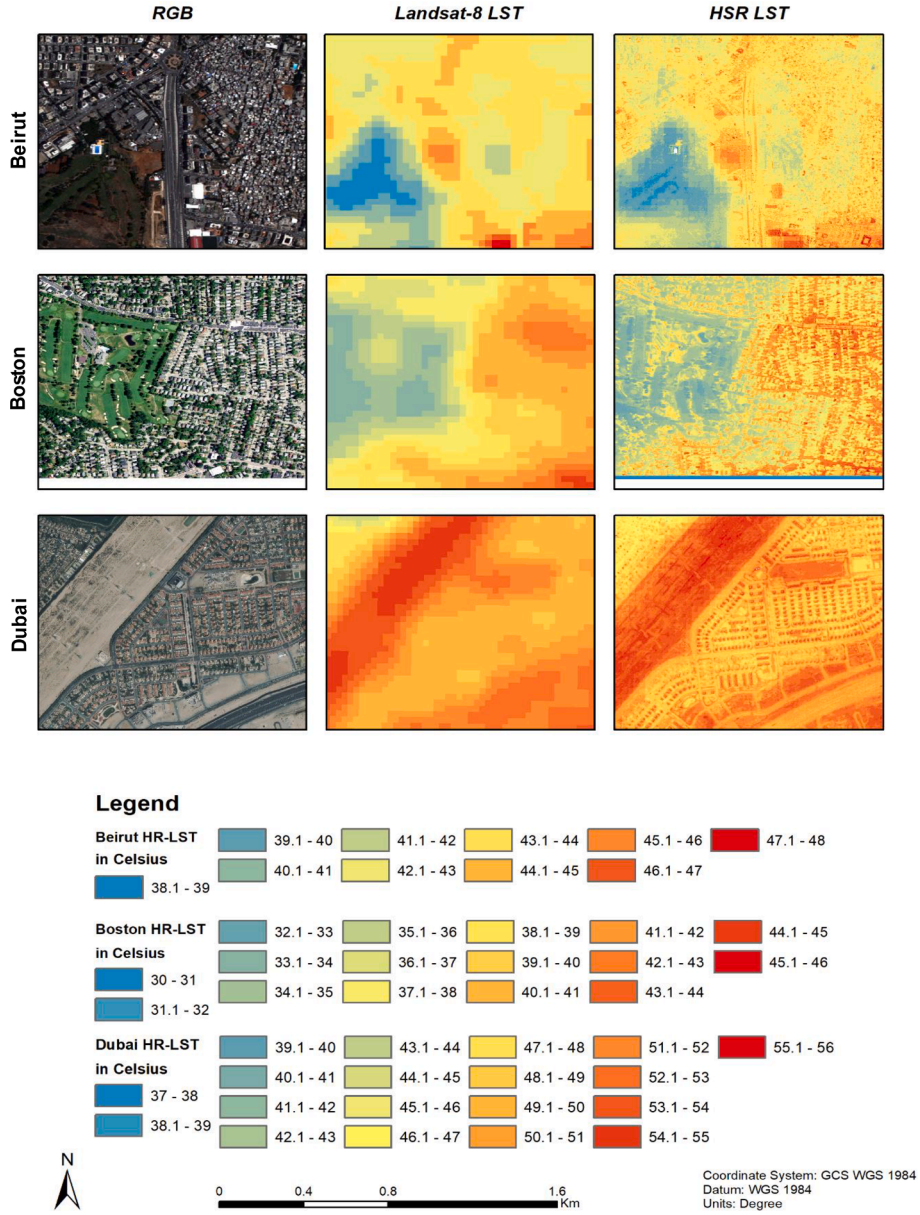

Fig. 7. A comparison between L8 LST and HSR-LST in, from top to bottom, Beirut (2-m LST), Boston (1-m LST) and Dubai (0.5-m LST).

open-source policies should be established to improve the sharing process of these HSR images for science and educational purposes. Of course, acquiring a larger number of HSR images would enable a better assessment of HSR-LST, particularly when considering different viewing angles or cloud-covered pixels. Future studies should focus on implementing such an approach in different cities with diverse climates across the Globe while providing more in-depth analysis of the findings. Sensitivity analysis can be conducted as well to check whether the median HSR image can be applicable for another few years. More importantly, as this study provides LST for the hot season based on the instantaneous thermal values captured by the L8 satellite at around 10:00 a.m. local time, applying HSR-LST using a geostationary satellite (e.g., [7,71]) or an unmanned aerial vehicle (e.g., [40,62]) would enable LSTs' hourly assessment and offer more advanced findings and recommendations. Furthermore, including other bands, such as the ShortWave InfraRed (SWIR), when available in high spatial resolution images, will enable further assessment of thermal properties for the different materials.

This study has demonstrated the variability of LST based on land cover and physical features resulting in LST increase or reduction based on specific urban features, which would not be apparent using the L8 LST. For example, the cooling effect of water and trees has decreased LST values, whereas, bare and grass lands showed an inverse impact. Urban configuration and buildings' material, density and height appear also to exhibit an effect on the local and surrounding LST values. Further studies should be conducted in that direction, especially with the availability of the reliable and automated HSR-LST downscaling system. Fine resolution data generated by the HSR-LST will provide community from policy makers to citizens with the necessary information to address rising temperatures in urban settings [28] and thus reducing the overall urban heat footprint while improving thermal comfort [34,61].

CRediT authorship contribution statement

Yaser Abunnasr: Conceptualization, Methodology, Writing - review & editing. **Mario Mhawej:** Conceptualization, Data curation, Formal analysis, Investigation, Methodology, Validation, Visualization, Writing - original draft, Writing - review & editing.

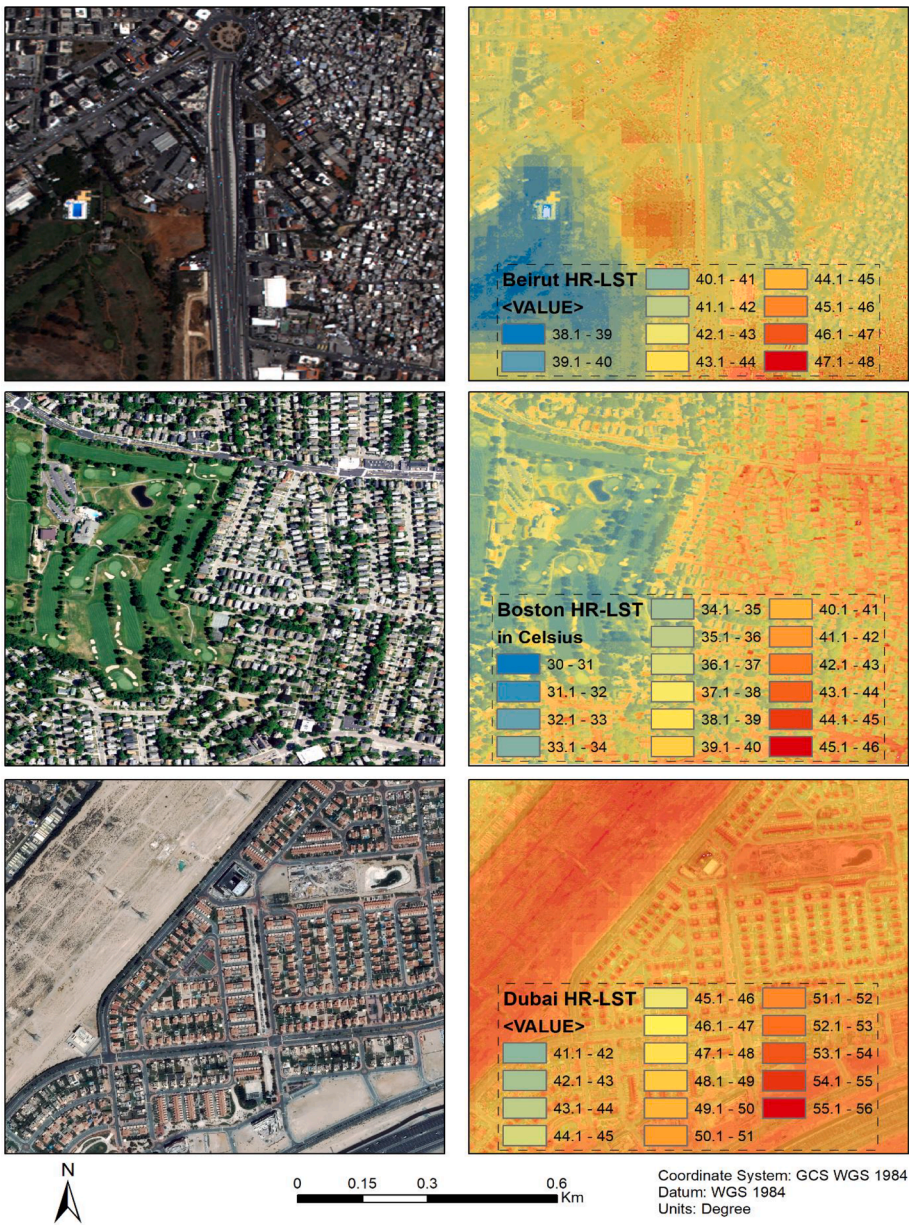

Fig. 8. Implementation of HSR-LST over, from top to bottom, Beirut, Boston and Dubai in the hot season.

Declaration of Competing Interest

The authors declare that they have no known competing financial interests or personal relationships that could have appeared to influence the work reported in this paper.

Data availability

I have shared the link in the manuscript

References

[1] Abunnasr Y, Mhawej M. Downscaled night air temperatures between 2030 and 2070: The case of cities with a complex-and heterogeneous-topography. Urban Clim 2021;40:100998.
[2] Abunnasr Y, Mhawej M. Pervious area change as surrogate to diverse climatic variables trends in the CONUS: A county-scale assessment. Urban Clim 2021;35:100733.
[3] Abunnasr Y, Mhawej M. Towards a combined Landsat-8 and Sentinel-2 for 10-m land surface temperature products: The Google Earth Engine monthly Ten-ST-GEE system. Environ Model Softw 2022;155:105456.
[4] Agam N, Kustas WP, Anderson MC, Li F, Neale CMU. A vegetation index based technique for spatial sharpening of thermal imagery. Remote Sens Environ 2007;107(4):545–58.
[5] Allam, Mona, Mario Mhawej, Qingyan Meng, Ghaleb Faour, Yaser Abunnasr, Ali Fadel, and Hu Xinli. Monthly 10-m evapotranspiration rates retrieved by SEBALI with Sentinel-2 and MODIS LST data.“ Agricultural Water Management XXX (2020): 105938.
[6] Bartesaghi-Koc C, Osmond P, Peters A. Spatio-temporal patterns in green infrastructure as driver of land surface temperature variability: The case of Sydney. Int J Appl Earth Obs Geoinf 2019;83:101903.
[7] Bechtel B, Zakšek K, Hoshyaripour G. Downscaling land surface temperature in an urban area: A case study for Hamburg, Germany. Remote Sens (Basel) 2012;4(10):3184–200.
[8] Bechtel B, Alexander PJ, Böhner J, Ching J, Conrad O, Feddema J, et al. Mapping local climate zones for a worldwide database of the form and function of cities. ISPRS Int J Geo Inf 2015;4(1):199–219.
[9] Bonafoni S. Downscaling of Landsat and MODIS land surface temperature over the heterogeneous urban area of Milan. IEEE J Sel Top Appl Earth Obs Remote Sens 2016;9(5):2019–27.
[10] Byerlay RAE, Nambiar MK, Amir Nazem Md, Nahian R, Biglarbegian M, Aliabadi AA. Measurement of land surface temperature from oblique angle airborne thermal camera observations. Int J Remote Sens 2020;41(8):3119–46.
[11] Carlson T. An overview of the“ triangle method” for estimating surface evapotranspiration and soil moisture from satellite imagery. Sensors 2007;7(8):1612–29.

[12] Cho K, Kim Y, Kim Y. Disaggregation of Landsat-8 thermal data using guided SWIR imagery on the scene of a wildfire. Remote Sens (Basel) 2018;10(1):105.
[13] Claverie M, Junchang Ju, Masek JG, Dungan JL, Vermote EF, Roger J-C, et al. The Harmonized Landsat and Sentinel-2 surface reflectance data set. Remote Sens Environ 2018;219:145–61.
[14] Cristóbal J, Jiménez-Muñoz JC, Prakash A, Mattar C, Skoković D, Sobrino JA. An improved single-channel method to retrieve land surface temperature from the Landsat-8 thermal band. Remote Sens (Basel) 2018;10(3):431.
[15] Demuzere M, Orru K, Heidrich O, El Olazabal D, Geneletti HO, Bhave AG, et al. Mitigating and adapting to climate change: Multi-functional and multi-scale assessment of green urban infrastructure. J Environ Manage 2014;146:107–15.
[16] Deng C, Changshan Wu. Estimating very high resolution urban surface temperature using a spectral unmixing and thermal mixing approach. Int J Appl Earth Obs Geoinf 2013;23:155–64.
[17] Dominguez A, Kleissl J, Luvall JC, Rickman DL. High-resolution urban thermal sharpener (HUTS). Remote Sens Environ 2011;115(7):1772–80.
[18] Dozier J. A method for satellite identification of surface temperature fields of subpixel resolution. Remote Sens Environ 1981;11:221–9.
[19] Du C, Ren H, Qin Q, Meng J, Zhao S. A practical split-window algorithm for estimating land surface temperature from Landsat 8 data. Remote Sens (Basel) 2015;7(1):647–65.
[20] Essa W, van der Kwast J, Verbeiren B, Batelaan O. Downscaling of thermal images over urban areas using the land surface temperature–impervious percentage relationship. Int J Appl Earth Obs Geoinf 2013;23:95–108.
[21] Faour G, Mhawej M. Mapping urban transitions in the Greater Beirut area using different space platforms. Land 2014;3(3):941–56.
[22] Faour, Ghaleb, Mario Mhawej, and Abbas Fayad. "Detecting Changes in Vegetation Trends in the Middle East and North Africa (MENA) Region Using SPOT Vegetation. Cybergeo: Eur J Geogr. (2016).
[23] Faour G, Mario M, Sandra AN. Regional landsat-based drought monitoring from 1982 to 2014. Climate 2015;3(3):563–77.
[24] Gao F, Kustas WP, Anderson MC. A data mining approach for sharpening thermal satellite imagery over land. Remote Sens (Basel) 2012;4(11):3287–319.
[25] Giglio L, Descloitres J, Justice CO, Kaufman YJ. An enhanced contextual fire detection algorithm for MODIS. Remote Sens Environ 2003;87(2–3):273–82.
[26] Guo G, Zhou X, Zhifeng Wu, Xiao R, Chen Y. Characterizing the impact of urban morphology heterogeneity on land surface temperature in Guangzhou, China. Environ Model Softw 2016;84:427–39.
[27] Guzinski R, Nieto H. Evaluating the feasibility of using Sentinel-2 and Sentinel-3 satellites for high-resolution evapotranspiration estimations. Remote Sens Environ 2019;221:157–72.
[28] Han Y, Taylor JE, Pisello AL. Toward mitigating urban heat island effects: Investigating the thermal-energy impact of bio-inspired retro-reflective building envelopes in dense urban settings. Energ Buildings 2015;102:380–9.
[29] Hobza CM, Strauch KR. Water-level and aerial thermal infrared imagery data collected along the lower Platte and Elkhorn Rivers, Nebraska, 2016-2017: U.S. Geological Survey data release 2019, https://doi.org/10.5066/P9EZLGSC.
[30] Hutengs C, Vohland M. Downscaling land surface temperatures at regional scales with random forest regression. Remote Sens Environ 2016;178:127–41.
[31] Jiang Y, Weng Q. Estimation of hourly and daily evapotranspiration and soil moisture using downscaled LST over various urban surfaces. GIScience Remote Sens 2017;54(1):95–117.
[32] Jing W, Yang Y, Yue X, Zhao X. A spatial downscaling algorithm for satellite-based precipitation over the Tibetan plateau based on NDVI, DEM, and land surface temperature. Remote Sens (Basel) 2016;8(8):655.
[33] Dialesandro JM, Wheeler SM, Abunnasr Y. Urban heat island behaviors in dryland regions. Environ Res Commun. 1(8);081005.
[34] Johansson E, Emmanuel R. The influence of urban design on outdoor thermal comfort in the hot, humid city of Colombo, Sri Lanka. Int J Biometeorol 2006;51(2):119–33.
[35] Khan MM, Chanussot J, Condat L, Montanvert A. Indusion: Fusion of multispectral and panchromatic images using the induction scaling technique. IEEE Geosci Remote Sens Lett 2008;5(1):98–102.
[36] Kustas WP, Norman JM, Anderson MC, French AN. Estimating subpixel surface temperatures and energy fluxes from the vegetation index–radiometric temperature relationship. Remote Sens Environ 2003;85(4):429–40.
[37] Li S, Jiang G-M. Land surface temperature retrieval from Landsat-8 data with the generalized split-window algorithm. IEEE Access 2018;6:18149–62.
[38] Liu D, Ruiliang Pu. Downscaling thermal infrared radiance for subpixel land surface temperature retrieval. Sensors 2008;8(4):2695–706.
[39] Maiti S, Satpathy R, Bandyopadhyay J, Jeyaseelan AT. Vegetation Parameter Derivation for Forest Health Measurement and Stress Detection in a Time Series. Res Rev J Ecol 2018;4(3):19–26.
[40] Malbéteau Y, Parkes S, Aragon B, Rosas J, McCabe MF. Capturing the diurnal cycle of land surface temperature using an unmanned aerial vehicle. Remote Sens (Basel) 2018;10(9):1407.
[41] Marzban F, Sodoudi S, Preusker R. The influence of land-cover type on the relationship between NDVI–LST and LST-T air. Int J Remote Sens 2018;39(5):1377–98.
[42] Meng X, Cheng J, Zhao S, Liu S, Yao Y. Estimating land surface temperature from Landsat-8 data using the NOAA JPSS enterprise algorithm. Remote Sens (Basel) 2019;11(2):155.
[43] Merlin O, Bitar AA, Walker JP, Kerr Y. An improved algorithm for disaggregating microwave-derived soil moisture based on red, near-infrared and thermal-infrared data. Remote Sens Environ 2010;114(10):2305–16.
[44] Merlin O, Duchemin B, Hagolle O, Jacob F, Coudert B, Chehbouni G, et al. Disaggregation of MODIS surface temperature over an agricultural area using a time series of Formosat-2 images. Remote Sens Environ 2010;114(11):2500–12.
[45] Mhawej M, Fadel A, Faour G. Evaporation rates in a vital lake: a 34-year assessment for the Karaoun Lake. Int J Remote Sens 2020;41(14):5321–37.
[46] Mhawej M, Abunnasr Y. Daily Ten-ST-GEE: An open access and fully automated 10-m LST downscaling system. Comput Geosci 2022;168:105220.
[47] Mhawej M, Caiserman A, Nasrallah A, Dawi A, Bachour R, Faour G. Automated evapotranspiration retrieval model with missing soil-related datasets: The proposal of SEBALI. Agric Water Manag 2020;229:105938.
[48] Mhawej M, Elias G, Nasrallah A, Faour G. Dynamic calibration for better SEBALI ET estimations: Validations and recommendations. Agric Water Manag 2020;230:105955.
[49] Mhawej M, Faour G, Fayad A, Shaban A. Towards an enhanced method to map snow cover areas and derive snow-water equivalent in Lebanon. J Hydrol 2014;513:274–82.
[50] Mhawej M, Faour G, Abdallah C, Adjizian-Gerard J. Towards an establishment of a wildfire risk system in a Mediterranean country. Eco Inform 2016;32:167–84.
[51] Nasrallah A, Baghdadi N, Mhawej M, Faour G, Darwish T, Belhouchette H, et al. A novel approach for mapping wheat areas using high resolution Sentinel-2 images. Sensors 2018;18(7):2089.
[52] Pan X, Zhu Xi, Yang Y, Cao C, Zhang X, Shan L. Applicability of downscaling land surface temperature by using normalized difference sand index. Sci Rep 2018;8(1):1–14.
[53] Peel, Murray C., Brian L. Finlayson, and Thomas A. McMahon. Updated world map of the Köppen-Geiger climate classification. (2007).
[54] Peng J, Loew A, Merlin O, Verhoest NEC. A review of spatial downscaling of satellite remotely sensed soil moisture. Rev Geophys 2017;55(2):341–66.
[55] Pour T, Miřijovský J, Purket T. Airborne thermal remote sensing: The case of the city of Olomouc, Czech Republic. Eur J Remote Sens 2019;52(sup1):209–18.
[56] Price JC. Combining multispectral data of differing spatial resolution. IEEE Trans Geosci Remote Sens 1999;37(3):1199–2120.
[57] Pu R, Bonafoni S. Reducing Scaling Effect on Downscaled Land Surface Temperature Maps in Heterogenous Urban Environments. Remote Sens (Basel) 2021;13(24):5044.
[58] Randerson JT, Liu H, Flanner MG, Chambers SD, Jin Y, Hess PG, et al. The impact of boreal forest fire on climate warming. Science 2006;314(5802):1130–2.
[59] Rozenstein O, Qin Z, Derimian Y, Karnieli A. Derivation of land surface temperature for Landsat-8 TIRS using a split window algorithm. Sensors 2014;14(4):5768–80.
[60] Sattari F, Hashim M, Pour AB. Thermal sharpening of land surface temperature maps based on the impervious surface index with the TsHARP method to ASTER satellite data: A case study from the metropolitan Kuala Lumpur, Malaysia. Measurement 2018;125:262–78.
[61] Sharmin T, Steemers K, Humphreys M. Outdoor thermal comfort and summer PET range: A field study in tropical city Dhaka. Energ Build 2019;198:149–59.
[62] Si M, Tang B-H, Li Z-L. Estimation of land surface temperature from unmanned aerial vehicle loaded thermal imager data. In: IGARSS 2018–2018 IEEE International Geoscience and Remote Sensing Symposium. IEEE; 2018. p. 1210–3.
[63] Skarbit N, Gál T, Unger J. Airborne surface temperature differences of the different Local Climate Zones in the urban area of a medium sized city. In: In 2015 Joint Urban Remote Sensing Event (JURSE). IEEE; 2015. p. 1–4.
[64] Stathopoulou M, Cartalis C. Downscaling AVHRR land surface temperatures for improved surface urban heat island intensity estimation. Remote Sens Environ 2009;113(12):2592–605.
[65] Tang R, Li Z-L, Tang B. An application of the Ts–VI triangle method with enhanced edges determination for evapotranspiration estimation from MODIS data in arid and semi-arid regions: Implementation and validation. Remote Sens Environ 2010;114(3):540–51.
[66] Wan Z, Li Z-L. A physics-based algorithm for retrieving land-surface emissivity and temperature from EOS/MODIS data. IEEE Trans Geosci Remote Sens 1997;35(4):980–96.
[67] Wang D, Chen Y, Leiqiu Hu, Voogt JA, Gastellu-Etchegorry J-P, Scott Krayenhoff E. Modeling the angular effect of MODIS LST in urban areas: A case study of Toulouse, France. Remote Sens Environ 2021;257:112361.
[68] Wang L, Tian F, Wang X, Yang Y, Wei Z. Attribution of the land surface temperature response to land-use conversions from bare land. Global Planet Change 2020;103268.
[69] Weng Q, Dengsheng Lu, Schubring J. Estimation of land surface temperature–vegetation abundance relationship for urban heat island studies. Remote Sens Environ 2004;89(4):467–83.
[70] Xu J, Zhang F, Jiang H, Hongda Hu, Zhong K, Jing W, et al. Downscaling ASTER land surface temperature over urban areas with machine learning-based area-to-point regression Kriging. Remote Sens (Basel) 2020;12(7):1082.
[71] Xu T, He X, Bateni SM, Auligne T, Liu S, Ziwei Xu, et al. Mapping regional turbulent heat fluxes via variational assimilation of land surface temperature data from polar orbiting satellites. Remote Sens Environ 2019;221:444–61.
[72] Yang C, Zhan Q, Lv Y, Liu H. Downscaling Land Surface Temperature Using Multiscale Geographically Weighted Regression Over Heterogeneous Landscapes in Wuhan, China. IEEE J Sel Top Appl Earth Obs Remote Sens 2019;12(12):5213–22.
[73] Yang G, Ruiliang Pu, Huang W, Wang J, Zhao C. A novel method to estimate subpixel temperature by fusing solar-reflective and thermal-infrared remote-sensing data with an artificial neural network. IEEE Trans Geosci Remote Sens 2009;48(4):2170–8.
[74] Yu X, Guo X, Zhaocong Wu. Land surface temperature retrieval from Landsat 8 TIRS—Comparison between radiative transfer equation-based method, split

window algorithm and single channel method. Remote Sens (Basel) 2014;6(10):9829–52.
[75] Yuan F, Bauer ME. Comparison of impervious surface area and normalized difference vegetation index as indicators of surface urban heat island effects in Landsat imagery. Remote Sens Environ 2007;106(3):375–86.
[76] Zakšek K, Oštir K. Downscaling land surface temperature for urban heat island diurnal cycle analysis. Remote Sens Environ 2012;117:114–24.
[77] Zhan W, Chen Y, Zhou Ji, Wang J, Liu W, Voogt J, et al. Disaggregation of remotely sensed land surface temperature: Literature survey, taxonomy, issues, and caveats. Remote Sens Environ 2013;131:119–39.
[78] Zhang X, Zhao H, Yang J. Spatial downscaling of land surface temperature in combination with TVDI and elevation. Int J Remote Sens 2019;40(5–6):1875–86.
[79] Zhao Z-Q, He B-J, Li L-G, Wang H-B, Darko A. Profile and concentric zonal analysis of relationships between land use/land cover and land surface temperature: Case study of Shenyang, China. Energ Build 2017;155:282–95.